Available online at www.sciencedirect.com
ScienceDirect
Organic Electronics 8 (2007) 487–497
Organic Electronics
www.elsevier.com/locate/orgel

Conductance switching, hysteresis, and magnetoresistance in organic semiconductors

J.H. Wei [a,*], S.J. Xie [a], L.M. Mei [a], J. Berakdar [b], YiJing Yan [c,*]

[a] School of Physics and Microelectronics, Shandong University, Jinan 250100, China
[b] Max-Planck Institut für Mikrostrukturphysik, 06120 Halle, Germany
[c] Department of Chemistry, Hong Kong University of Science and Technology, Kowloon, Hong Kong, China

Received 5 November 2005; received in revised form 27 January 2007; accepted 28 February 2007
Available online 12 March 2007

Abstract

The controllability of charge transport through an organic molecular spin-valve system is theoretically investigated on the basis of a Su–Schrieffer–Heeger model combined with the non-equilibrium Green's function formalism. We show how the formation of polaron in the organic sub-structure leads to a hysteretic conductance switching, via sweeping either the bias voltage or the electrochemical potential. We further obtain an exponential dependence of the magnetoresistance as a function of the applied bias voltage. The implications of calculated results in relation to experiments and device applications are addressed and commented.

PACS: 85.75.−d; 73.61.Ph; 71.38.Ht

Keywords: Conductance switching; Hysteresis; Giant magnetoresistance; Organic spintronics

1. Introduction

Due to their compatibility in processing and tunability in electronic properties, π-conjugated organic semiconductors (OSEs) have been utilized broadly for various device applications [1–5]. Recent progress in the field of OSE electronics has revealed a number of technologically important transport characteristics, such as current rectification [6], Coulomb blockade [7], Kondo resonance [8], negative differential resistance (NDR) [9–12], bistable switching [13–19], and giant magnetoresistance [20,21].

An OSE system is characterized by not only its electronic structure but also its strong electron–phonon (e–ph) coupling that induces polarons [22,23]. In view of charging-induced conformational change [14,24], the formation of non-equilibrium polaron should be a reasonable mechanism of the conductance switching and/or NDR in OSE electronics. This idea is first shown theoretically by Galperin et al. [25] with a simplified model, in which the molecular wire consists of a single electronic state coupled with a single Brownian oscillator.

* Corresponding authors.
E-mail addresses: wjh@sdu.edu.cn (J.H. Wei), yyan@ust.hk (Y. Yan).

1566-1199/$ - see front matter © 2007 Elsevier B.V. All rights reserved.
doi:10.1016/j.orgel.2007.03.002

Apparently, the Su–Schrieffer–Heeger (SSH) model [26] renders a more realistic description of an OSE system. It captures the essential characteristic of a conjugated molecule, where the strong e–ph coupling leads it to the polaron charged states and dimerized ground state. Indeed, the SSH model has been remarkably successful in the study of the electronic conductivity and optical phenomena in π-conjugated OSEs. In addition to conducting polymers, the SSH model has also been extended to molecular systems [27,28], carbon nanotubes [29], and DNA molecules [30]. We have recently [31] exploited this model for an OSE system, and demonstrated that a NDR may appear due to the annihilation of a predoped polaron; i.e., an equilibrium charge transfer state that may exist before applying the external bias voltage. The resulting NDR can also be spin-polarization sensitive, leading to a magnetoresistance significantly larger than 100%.

In this work, we elucidate the possibility of a polaron mechanism for the bistable switching and hysteresis in OSE nanostructures, and further for the giant magnetoresistance in OSE spin-valve devices where ferromagnetic metal electrodes are used. More importantly, we highlight that these technologically important properties are likely achievable by a wide range of OSE systems. To do that, moderate/typical values of the SSH parameters will be adopted in this work to avoid the formation of predoped polarons mentioned earlier. Besides the model and its parameters for the OSE spin-valve nanostructure of study, Section 2 presents also the transport theory based on the Keldysh non-equilibrium Green's function (NEGF) formalism [32–34], together with its implementation to the evaluation of current in response to linear sweeping bias voltage. Hysteretic conductance switchings controlled via bias voltage and via an electrochemical means are then numerically investigated in Sections 3 and 4, respectively. The giant magnetoresistance property of OSE spintronic structures is addressed in Section 5. Finally, we conclude in Section 6.

2. Model and theory

2.1. A Su–Schrieffer–Heeger static polaron model

We adopt a non-degenerate SSH Hamiltonian for the isolate OSE system [20,30],

$$H_{\mathrm{OSE}} = \sum_{n,\sigma}\{\epsilon_0 c^+_{n,\sigma}c_{n,\sigma} - [t_0 - (-1)^n t_1 - \alpha_0(u_{n+1} - u_n)] \times (c^+_{n,\sigma}c_{n+1,\sigma} + c^+_{n+1,\sigma}c_{n,\sigma})\} + \frac{K_0}{2}\sum_n (u_{n+1} - u_n)^2. \quad (1)$$

Here, $c^+_{n,\sigma}$ ($c_{n,\sigma}$) denotes the creation (annihilation) operator of an electron at the nth site with spin σ of the OSE system. The e–ph coupling induced on-site lattice displacement parameters $\{u_n\}$ are treated classically and will be determined in a self-consistent manner to be described later (cf. Section 2.2). The input parameters involved in Eq. (1) are the on-site energy ϵ_0, zero-displacement hopping integral t_0, non-degeneracy parameter t_1, electron–phonon coupling α_0, and lattice elastic constant K_0.

For the electrodes, we choose two symmetrical 3d ferromagnetic (FM) transition metals; each of them is described by a one-dimensional tight-binding Hamiltonian with the Stoner-like exchange term [35],

$$H_{\mathrm{FM}} = \sum_{n,\sigma}\{\epsilon_{\mathrm{f}} d^+_{n,\sigma}d_{n,\sigma} + t_{\mathrm{f}}(d^+_{n,\sigma}d_{n+1,\sigma} + d^+_{n+1,\sigma}d_{n,\sigma})\} - \sum_n J_{\mathrm{f}}(d^+_{n,\uparrow}d_{n,\uparrow} - d^+_{n,\downarrow}d_{n,\downarrow}). \quad (2)$$

Here, $d^+_{n,\sigma}$ ($d_{n,\sigma}$) denotes the creation (annihilation) operator of a 3d-electron at the nth site with spin σ of the metal electrode; ϵ_{f} is the on-site energy of a metal atom, t_{f} the nearest neighbor transfer integral, and J_{f} the Stoner-like exchange integral.

The coupling between the OSE and each of the FM electrodes is described by a tight-binding hopping integral,

$$t_{\mathrm{c}} = \beta(t_{\mathrm{f}} + t_0). \quad (3)$$

Here, β is the OSE–FM binding parameter, which for simplicity is set to be spin-independent. However, charge transport can be spin dependent. According to the two-current description, the total current arises from the majority-spin (up-spin) and the minority-spin (down-spin) of the 3d electrons of the FM electrodes [36]. We also neglect the spin-flip processes during the spin-dependent charge transport that takes place between the FM electrodes.

The above simple model for the molecule–metal coupling allows us to focus on the effects of OSE molecular system on the spin-dependent transport.

2.2. Non-equilibrium Green's function formalism

The quantum transport, in terms of the conductance switching, hysteresis and giant magnetoresistance behaviors of the model FM/OSE/FM system, will be calculated by means of the NEGF approach, based on the Keldysh formalism [5,32–34]. To proceed, the infinite FM/OSE/FM system is divided into three distinct regions: The central scattering region (S) that consists of the OSE together with a few metal atoms attached to each of its ends [34], and two semi-infinite FM electrodes (L and R) that serve as charge reservoirs and also set the temperature and electron distribution of the junction in the steady state. As results, the Hamiltonian for the whole system is mapped onto a 3×3 block matrix,

$$H_{\rm total}=\begin{pmatrix} H_{\rm L} & H_{\rm LS} & 0\\ H_{\rm SL} & H_{\rm S} & H_{\rm SR}\\ 0 & H_{\rm RS} & H_{\rm R}\end{pmatrix}, \tag{4}$$

with $H_{\rm L}$, $H_{\rm S}$, and $H_{\rm R}$ being the isolated Hamiltonians for the L-electrode, the central scattering S-region, and the R-electrode, respectively, while $H_{\rm LS}=H_{\rm SL}^{\dagger}$ and $H_{\rm RS}=H_{\rm SR}^{\dagger}$ the couplings between them.

The applied electric potential bias V does not change the electronic structure of L and R leads, but just shifts their energy levels by $eV/2$ and $-eV/2$, respectively. This leads to the electron distribution function $f(E,\mu_\alpha)\equiv[{\rm e}^{(E-\mu_\alpha)/k_{\rm B}T}+1]^{-1}$, where $\mu_{\rm L/R}=\mu_{\rm eq}\pm eV/2$, with $\mu_{\rm eq}=E_{\rm F}$ being the Fermi energy of the FM electrode. In contrast to the electrodes, the effect of applied bias on the S-region is characterized by the electric potential function $\Phi(x)$. With the boundary conditions of $\Phi(x_1)=V/2$ and $\Phi(x_{N_{\rm S}})=-V/2$, it shifts the nth-site energy by $-e\Phi(x_n)$ in the S-region. As it is correlated with the electronic and lattice structures of OSE, $\Phi(x)$ should be evaluated together with the S-region density matrix and lattice distortion in a self-consistent manner, which will be elaborated soon [cf. Eqs. (10)–(12)].

Eliminating the L- and R-electrodes degrees of freedom results in the NEGF of the central S-region [33],

$$G(E)=\frac{1}{E-H_{\rm S}+e\Phi(x)-\sum_{\rm L}(E)-\sum_{\rm R}(E)+{\rm i}0_+}. \tag{5}$$

The effect of L- or R-electrode coupling is incorporated via the self-energy,

$$\sum_{\alpha}(E)=H_{{\rm S}\alpha}\frac{1}{E-H_\alpha+{\rm i}0_+}H_{\alpha{\rm S}};\quad \alpha={\rm L},\ {\rm R}. \tag{6}$$

In particular, $\Gamma_{\rm L/R}(E)\equiv{\rm i}[\sum_{\rm L/R}(E)-\sum_{\rm R/L}^{\dagger}(E)]$ amounts to the electrode coupling-induced broadening function.

The electron transmission probability function reads in terms of the NEGF at a finite bias as [33]

$$T(E,V)={\rm Tr}[\Gamma_{\rm L}(E)G(E)\Gamma_{\rm R}(E)G^{\dagger}(E)]. \tag{7}$$

The electric current can then be evaluated as [33,37,38]

$$I=\frac{2e}{h}\int_{-\infty}^{\infty}T(E,V)[f(E,\mu_{\rm L})-f(E,\mu_{\rm R})]\,{\rm d}E. \tag{8}$$

We shall show later that the above expression remains practically valid in the evaluation of current under the quasi-steady-state voltage sweeping condition; cf. the comments to the end of this subsection.

The NEGF determines also the density of states $D(E)$ and the density matrix ρ in the S-region [34]. They are given, respectively, by

$$D(E)=\frac{\rm i}{2\pi}{\rm Tr}[G(E)-G^{\dagger}(E)], \tag{9}$$

and

$$\rho=\frac{1}{2\pi}\sum_{\alpha={\rm L,R}}\int_{-\infty}^{\infty}f(E,\mu_\alpha)[G(E)\Gamma_\alpha(E)G^{\dagger}(E)]\,{\rm d}E. \tag{10}$$

The number of carrier electrons in the S-region is $N={\rm Tr}(\rho S)$, with S denoting the overlap integral matrix that reduces to the unit matrix if an orthogonal basis set is used.

We are now in the position to complete the self-consistent evaluation of the NEGF. The involving electric potential function $\Phi(x)$ in Eq. (5) is related to the charge density, and the latter depends further on the steady-state lattice distortion at a given finite applied electric potential bias.

Let us start with the Poisson equation that relates $\Phi(x)$ and the on-site charge $\{\rho_{nn}\}$,

$$\nabla^2\Phi(x)=-\sum_n\frac{\rho_{nn}}{\varepsilon_0}\delta(x_n-x). \tag{11}$$

Here, ε_0 denotes the vacuum permittivity, and $x_n=(n-1)a+u_n$, with a being the e–ph coupling-free lattice constant and set to be 0.122 nm. The e–ph coupling-induced on-site lattice displacement is of the boundary conditions of $u_1=u_{N_0}=0$. To solve the Poisson equation we introduce $\Phi(x)=$

$(0.5 - x/L)V + \delta\Phi(x)$, with L denoting the S-region length. $\delta\Phi(x)$ satisfies the same Poisson equation, but with the boundary conditions of $\delta\Phi(x_1) = \delta\Phi(x_{N_0}) = 0$. It can be readily evaluated in terms of the on-site charge $\{\rho_{nn}\}$ via the method of images, in which $\delta\Phi(x)$ is a sum of the individual image contributions from all point charges. To avoid the infinity associated with point charges, we follow the Appendix 3 of Ref. [39] and analytically integrate the usual electrostatic potential within the small area around each point charge separately.

Consider now the lattice distortion, which plays an important role in determining the properties of OSE due to the strong e–ph interactions. For a steady or quasi-steady state, the lattice distortion is assumed to catch up with the variation of charges under a slow voltage sweep condition treated in this work. In this case, the OSE lattice distortion can be determined in terms of the density matrix elements via the Hellman–Feynman variation theorem of $0 = \partial E_S/\partial u_n = \partial \mathrm{Tr}(H_S\rho)/\partial u_n$. It is that

$$2\alpha_0(\rho_{n,n-1} - \rho_{n+1,n}) + K_0(2u_n - u_{n-1} - u_{n+1}) = 0. \tag{12}$$

Eqs. (10)–(12) constitute a set of coupled equations for solving ρ, $\Phi(x)$ and $\{u_n\}$ in a self-consistent manner by iteration. The converged result in the electric potential $\Phi(x)$ is then used to determine the NEGF of Eq. (5), and then the I–V characteristics of Eq. (8). The most time consuming part of the aforementioned self-consistent evaluation is Eq. (10). The involving integrand is non-zero over a broad energy range and often has sharp structures that makes Eq. (10) numerically challenging. To facilitate this problem, let

$$\rho \equiv \rho_{\mathrm{eq}} + \delta\rho, \tag{13}$$

where

$$\rho_{\mathrm{eq}} = \frac{1}{2\pi}\sum_{\alpha=\mathrm{L,R}}\int_{-\infty}^{\infty} f(E,\mu_{\mathrm{eq}})[G_{\mathrm{eq}}(E)\Gamma_\alpha(E)G_{\mathrm{eq}}^\dagger(E)]\,\mathrm{d}E \tag{14}$$

is the equilibrium density matrix, and $\delta\rho$ the non-equilibrium correction. The evaluation of ρ_{eq} requires a broad energy range and couples only with Eq. (12) as $V = 0$ is implied. The involving integration will be tackled by taking the advantage of the contour integration technique [34,40]. On the other hand, the non-equilibrium correction $\delta\rho$ involves the self-consistent determination, together with Eqs. (11) and (12). It will be evaluated directly, as the integration is now required only for a limited energy range, where the integrands in Eqs. (10) and (14) differ significantly. This is the same situation as the evaluation of current [Eq. (8)], and can thus be carried out with a fine grid. Note that ρ_{eq} is naturally real but $\delta\rho$ may not, unless a real basis set functions is employed. This is the case of this work, and the resulting ρ does assume a real matrix.

To conclude this subsection, let us comment on the quasi-steady-state condition that will be applied in this work for the evaluation of I–V characteristics subject to a sweeping voltage of $V(t) = V_0 \pm V't$. Here, $V_0 = 0$ or $V_{\max}$ for the sweeping up (+) or down (−) direction, respectively; $V' > 0$ denotes the constant rate of bias sweeping, which is typically 0.01–0.1 V/s in experiments. In our calculations of the quasi-steady-state current of interest, we set $V' = 0.1$ V/s. Note that all experimental observations of the correlated electron and lattice degrees of freedom on the OSE are functionals of density matrix ρ. As the bias sweeping is linear, one can map the time evolution of density matrix onto the bias sweeping one, $\rho(t) \to \rho(V)$. Starting from $\rho(t = 0)$, the density matrix evolution is then evaluated via $\rho(t + \Delta t) = \rho(t) + \langle\Delta\rho(t)\rangle_T$, where the second term denotes the time average of $\Delta\rho(t)$ over the range of $[t,t + T]$. with T being the measurement duration (set to be $T = 1$ s) under the quasi-steady-state condition. The corresponding $I(t) \to I(V)$ in each of the measurement time interval is then formally the same as Eq. (8).

2.3. Model parameters

Reasonable values for the model parameters must be determined from other sources, such as the band structure calculations and/or experimental current–voltage (I–V) characteristics. In this study, the FM electrodes are chosen to be cobalt metal. With its experimental 3d-band structure and Fermi energy of $E_F = -4.9$ eV [21,41], the tight-binding parameters for the Co metal in Eq. (2) are determined as $t_f = 1.5$ eV, $J_f = 1.45$ eV, and $\epsilon_f = -6.5$ eV. The parameters of the OSE in Eq. (1) are chosen as $\epsilon_0 = -5.5$ eV, $t_0 = 2.5$ eV, $t_1 = 0.04$ eV, $\alpha_0 = 5.0$ eV/Å, and $K_0 = 21.0$ eV/Å^2. These are the modified values from those of a typical conducting polymer, but lead to a relatively large band gap, which is about 2.8 eV for the OSE length of $N_0 = 10$ sites considered in this work. In a realistic OSE molecule, the on-site energy ϵ_0 can

be site-dependent and also can be adjusted by applying a gate voltage [4]. The OSE–Co metal binding parameter β affects the magnitude of current sensitively, but it is hardly controlled due to the weak interaction. In the calculations, one can adjust it so that the calculated I–V curve is of about the same amplitude of the measured one. We find that choosing $\beta = 0.25$ for the conductance switching via applied voltage sweep and $\beta = 0.5$ for that via electrochemical potential sweep will produce the current in the magnitude of nA for some nanosize molecules reported experimentally [13–19].

For a self-consistent evaluation of quantum transport based on the NEGF formalism, the central scattering S-region is chosen such that its Green's function can properly represent the bulk property at the boundary. For the coupling parameters given above, it is sufficient to have the S-region a total of $20 + 10 + 20$ sites; i.e., to include 20 Co electrode atoms to each end of the model OSE of length $N_0 = 10$. For the OSE–Co binding parameter used in this work, it is found that the OSE subsegment is charge neutral in the absence of applied bias ($V = 0$). Changing the relative energy levels of OSE with respect to electrodes may lead to intra-regional charge transfer, forming a preexisting (charged) polaron state in the OSE before applying bias voltage [31].

Fig. 1 depicts the band structures of the OSE and the Co metal electrodes at a low temperature ($T = 11$ K). This figure summarizes the model parameters adopted in this work (except for β which in this figure is set to zero). For the OSE, the evaluated band gap is about 2.8 eV, which well reproduces the band diagram of the organic spin-valve system in a recent experiment [21]. For the Co electrodes, our calculation is consistent with the real material [41], showing a completely filled 3d band and a half-filled 3d band for the majority-spin (up-spin) and the minority-spin (down-spin) electrons, respectively.

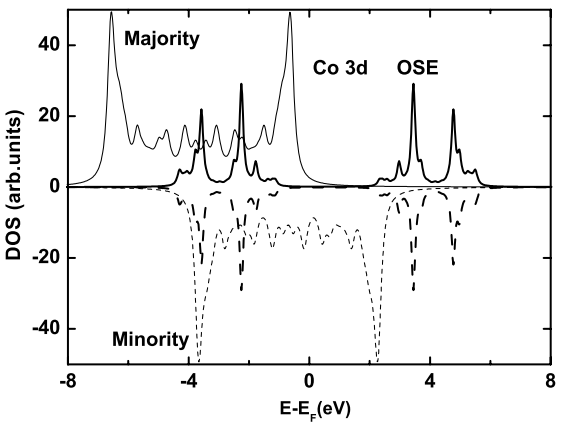

Fig. 1. Density of states of Co 3d band and OSE structure at 11 K. The solid (dashed) lines correspond to majority (minority) electronic bands. The thick (thin) curves are for OSE (Co), with the phenomenological Lorentzian width of 0.15 eV being included.

Quantitative simulations of experiment results [21,42–44] may need to incorporate the spin dynamics, such as spin-flip, diffusion and accumulation, which are however not included in this work. Despite of its simplicity, we shall show soon that the present model possesses some interesting properties that can highlight the important transport mechanism in relation to experiments.

3. Hysteretic conductance switching via bias voltage sweep

In this section we report the hysteretic bistable switching I–V behavior of the model Co/OSE/Co structure. In contact with experimental reality [13,18], the bias sweep rate in our calculations is fixed at a representing value of 0.1 V/s, at which the quasi-steady-state condition is reasonably satisfied.

There are two distinct transport measurement configurations, parallel (P) and antiparallel (AP), with respect to the relative magnetization orientation of two FM electrodes. Generally, in the two-current model, both the majority–majority and minority–minority (or majority–minority and minority–majority) transports are permitted in the P (or AP) configuration. However, for the cobalt electrodes in the present work, the full-filled up-spin electrons cannot transport in P-configuration under a positive bias voltage $V > 0$ and the charge carriers are only the half-filled down-spin electrons. Contrary, the charge carriers in AP-configuration under $V > 0$ are only the up-spin electrons, driven from the full-filled majority-spin band of L-electrode to the half-filled minority-spin band of R-electrode of opposite magnetization orientation.

Fig. 2 depicts the resulting hysteretic I–V characteristic in P-configuration. The bias sweep directions are indicated with the arrows. The OSE nanostructure is shown to have an insulating state and two conducting states in the indicated sweeping bias range. These conducting states are switched on (off), respectively, at 1.5 ± 0.2 V (0.75 ± 0.2 V)

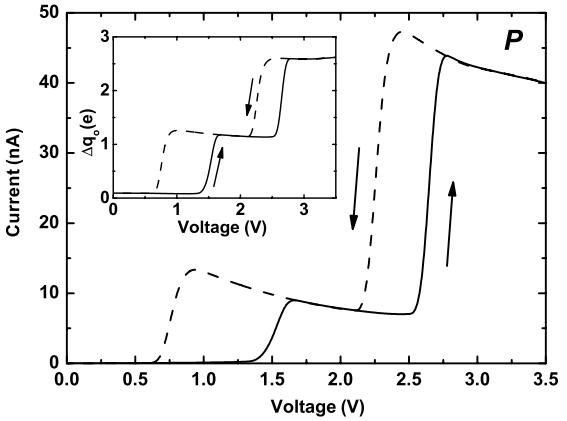

Fig. 2. The hysteretic current as the function of sweeping bias potential for the model OSE in junction with Co electrodes in the parallel configuration. The linear voltage sweep rate is at 0.1 V/s. The inset is the bias voltage-induced charge variation in the OSE substructure. The OSE–Co metal binding parameter $\beta = 0.25$.

and 2.6 ± 0.1 V (2.1 ± 0.1 V) in the sweep up (down) direction. The voltage-triggered two-step hysteretic conductance switching has been observed experimentally in some molecular nanojunction systems [18], often associating with voltage-triggered molecular confirmation change. On the other hand, that observed in Fig. 2, according to the e–ph coupling Hamiltonian used here (cf. Section 2), can only be of polaron in nature. The inset in Fig. 2 shows the sweeping bias-induced charge modification Δq_0 within the OSE sub-structure. The synchronization between the Δq_0–V and I–V curves demonstrates clearly that the two voltage-triggered conducting states have $1.15e$ and $1.44e$ charges, respectively. These are negatively charged polaron states, with the clear evidence of the e–ph coupling induced lattice distortion being presented soon (cf. Fig. 3).

To further elaborate what happens to the conductance bistability of the OSE nanostructure, Fig. 3 depicts the transmission function and lattice distortion for the bistable states, exemplified with the P-configuration at $V = 1$ V (cf. Fig. 2). The resulting window between μ_L and μ_R for the electric transmission $T(E)$, as indicated in Fig. 3a, clearly distinguishes between the conducting state (solid curve) and the insulation state (dash curve). Note that the lattice distortions in Fig. 3b are reported in terms of the e–ph coupling induced bond length variation $y_n = u_{n+1} - u_n$ between nearest neighbors. The dashed curve there for the insulating state is effectively the same as the equilibrium ($V = 0$)

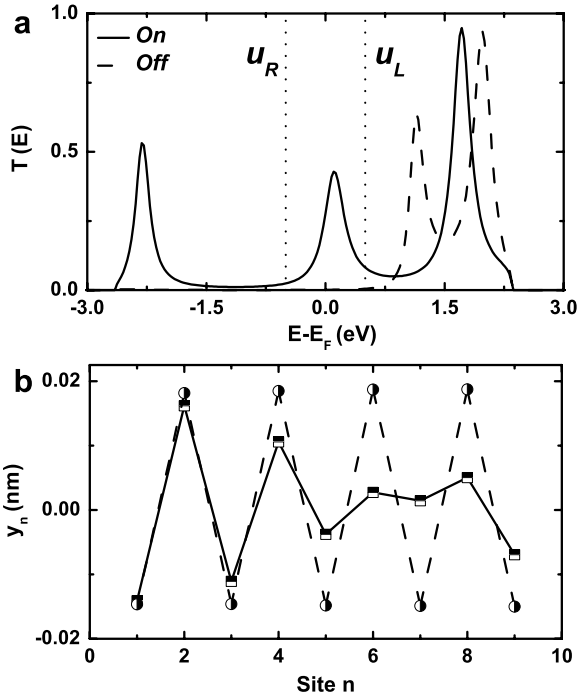

Fig. 3. Bistable switched-on (solid-curves) and switched-off (dashed-curves) states for the P-configuration at bias voltage $V = 1.0$ V. (a) Transmission coefficient of down spin electrons. The vertical dot lines indicate the window between μ_L and μ_R for the charge transmission. (b) Lattice distortion $y_n \equiv u_{n+1} - u_n$ of the OSE substructure.

lattice distortion. In contrast, the solid curve in Fig. 3 demonstrates that a charged polaron state is formed in the conducting state toward the right-side of the OSE-substructure due to the external bias-induced spatial symmetry broken.

The polaron mechanism for the observed hysteretic conduction switching behavior in Fig. 2 can now be summarized as follows. In the equilibrium state ($V = 0$), the OSE substructure is charge neutral, with its lowest-unoccupied and highest-occupied molecular orbital (LUMO and HOMO) electronic wave functions delocalized over the entire S-region. The chemical potentials of electrodes are the same as the Fermi energy, $\mu_L = \mu_R = E_F$, locating in between the LUMO and HOMO levels of the OSE; no current is observed and the OSE is in an insulating state. Applying a positive bias $V > 0$, which elevates $\mu_L = E_F + eV/2$ and depresses $\mu_R = E_F - eV/2$, drives electron transport from L-electrode to R-electrode through the unoccupied levels of OSE substructure. Since the two bistable conductance states in Fig. 2 are of the same physical origin, let us focus on the first one for illustration.

As the sweep-up voltage approaches to the vicinity of the LUMO level, electron starts to migrate into the OSE, followed by the e–ph coupling-induced reorganization that leads to the formation of polaron. In other words, $V_{on} = 2(E_{LUMO} - E_F)/e$ defines the switch-on voltage of the first conducting state. However, as the OSE gets charged, the e–ph coupling-induced reorganization process occurs, forming a polaronic gap state that serves as the first conducting state in Fig. 2. The fact that $E_{polaron} < E_{LUMO}$ due to the reorganization accounts therefore for the observed hysteresis, since $V_{off} = 2(E_{polaron} - E_F)/e$ is the switch-off voltage in the down-sweep direction. In the case of study here, $V_{on} \approx 1.5$ V and $V_{off} \approx 0.75$ V (cf. Fig. 2). The reorganization energy of the negatively charged polaron gap state can be obtained as $E_{LUMO} - E_{polaron} = e(V_{on} - V_{off})/2 \approx 0.37$ eV.

Fig. 4 depicts the hysteretic I–V characteristics and the corresponding charge modifications for the AP-configuration of the electrode magnetization directions. Similar to the P-configuration, the two-step hysteretic conductance switching behavior appears also here. This observation indicates that the hysteresis itself is originated from the OSE due to the polaron formation, regardless the contact is magnetic and nonmagnetic in this aspect. However, in the present Co/OSE/Co model study, the hysteresis curves in the AP-configuration are narrower than those in the P-configuration. This difference gives us an additional handle by using a magnetic contact on the conductance control since one can alter from the P- to the AP-configuration of magnetization by applying an external magnetic field, especially when the electrode is made of soft magnetic material.

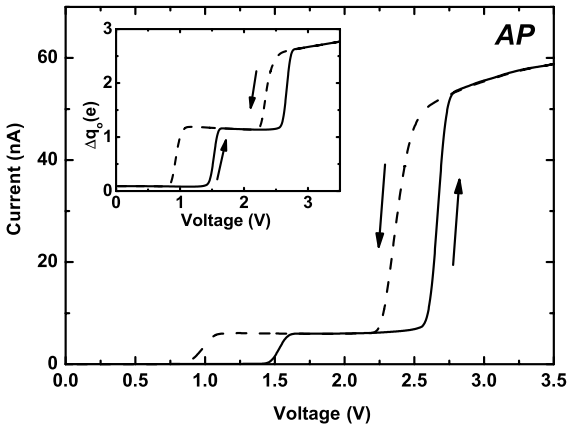

Fig. 4. Same as Fig. 2 but for the antiparallel configuration of the Co electrodes.

4. Hysteretic conductance switching via electrochemical potential sweep

We now turn to another type of conductance switching, controlled by sweeping the Fermi energy [or ϵ_f effectively in Eq. (2)] of both electrodes simultaneously via an electrochemical means, or equivalently sweeping the gate voltage via an microelectronic means that adjusts the on-site energy of the OSE. Here, the bias voltage is kept fixed at a small value to open a transmission window between μ_L and μ_R. For instance, in the experiment of He et al. [18], the current through Au–polyaniline–Au nanoelectronic junctions was measured under a linear sweep of the electrochemical potential at a fixed bias voltage of 20 mV. The fast conductance switching behaviors of the electrochemical system is closely related to chemical and biosensor applications [18,45], while the gate voltage modulation is of great importance for the organic transistors and memories [16,46]. They share the same mechanism; i.e. the control of the polaron (reduced/oxidized) state of the molecule by electrochemical potential or gate voltage, and can therefore be qualitatively illustrated with the same model. As discussed earlier, the polaron formation is responsible to the conductance switching. It arises from the coupling between the electronic states of the OSE near the LUMO energy and that of the metal leads near μ_α ($\alpha = L, R$). When μ_α approaches to the polaron energy level (which is lower than the LUMO of the ground state) an abrupt change of current occurs.

In the following calculations, we fix the electrochemical potential sweeping rate at 0.1 eV/s that supports the quasi-steady-state condition. As described to the end of Section 2.2, Eq. (8) together with Eqs. (10)–(12) are used again for the evaluation of the quasi-steady-state current as the time-averaged one in the interval of every second.

Fig. 5 shows the dependence of the charge transport current on a sweeping of the electrochemical potential E_P, in terms of its difference from the initial Fermi level E_F (=4.9 eV) of the metal leads in the P-configuration of electrodes. The bias voltage between the electrodes is kept at a constant value of 20 mV. The OSE–Co metal binding parameter is $\beta = 0.25$ in Fig. 5a and $\beta = 0.5$ in Fig. 5b, respectively. While the value of β affects the magnitude of

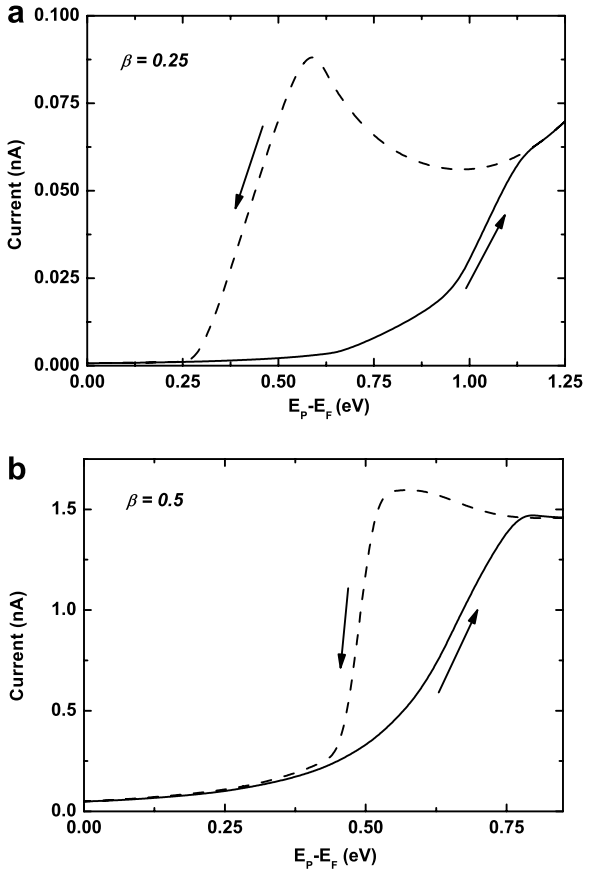

Fig. 5. The hysteretic current as the function of sweeping electrochemical potential for the model OSE in junction with Co electrodes in the parallel configuration, at the fixed bias voltage of $V = 20$ mV. The OSE–Co binding parameter: (a) $\beta = 0.25$ and (b) $\beta = 0.5$, respectively. The initial Fermi level $E_F = 4.9$ eV.

current, the hysteretic behavior of conductance switching is shown to be an intrinsic character of the OSE, regardless the details of OSE–electrode coupling. Making in contact with the experimental output of current, which is of nA in magnitude for a nanosized molecule [16,18], $\beta = 0.5$ is favored for the calculations of the potential-dependent conductance switching behavior.

As shown in Fig. 5b, enhancing the potential leads to a rapid increase of the current during $E_P - E_F \sim 0.5$ eV and 0.75 eV, as the OSE switches from the insulating to the conducting state. The hysteresis behavior here is attributed to the formation of a *bipolaron* state that localizes two electrons in the OSE region. The formation of a bipolaron (not depicted here) is further confirmed with various OSE chain lengths of $N_0 = 10$–40.

The electrochemical potential-dependent charge transport behavior is similar to its bias voltage-dependent counterpart. In both cases, the same physical mechanism; i.e., the polaron-assisted charge transport is operational. A similar phenomenon is also found for the AP-configuration of electrodes.

The potential dependent spin-polarized charge transport through OSE has been studied theoretically by Xie et al. [35] in the context of the ground-state properties of ferromagnetic metal/conjugated polymer interface. The conclusions there are that electrons can transfer to the polymer and form bipolarons from the magnetic layer through an interfacial coupling by adjusting the relative chemical potentials of the contact and the polymer. This conjecture is confirmed by the present calculations.

5. Magnetoresistance effects

Now we address the magnetoresistance property of the model Co/OSE/Co spin-valve system, measured as

$$\mathrm{MR} = \frac{R_{\mathrm{AP}} - R_{\mathrm{P}}}{R_{\mathrm{AP}}}. \tag{15}$$

Here, R_{AP} (R_{P}) denotes the electric resistance with the antiparrellel (parallel) magnetization orientation of two FM electrodes. To study that, we turn on the conductance of OSE by choosing $E_P = E_F + 0.8$ eV (cf. Fig. 5), and calculate the steady-state currents [Eq. (8) with Eqs. (10)–(12)]. The resulting I–V characteristics of the model Co/OSE/Co spin-valve device in the conducting state for both the P- and AP-configurations of electrodes are shown in Fig. 6, and the corresponding MR behavior in the inset. The I–V characteristics for the P-configuration exhibits roughly a linear behavior (with $R_P \approx 17$ MΩ) and can be considered as a metallic phase. In contrast, for the AP-configuration the current increases much slower and is non-linear as the bias voltage increases. The resulting MR shown in the inset of Fig. 6 decays nearly exponentially as the applied bias voltage increases from $V = 0$ where MR ≈ 100% to $V = 0.5$ V where MR = 60%. The relatively large MR here in comparing with the typical experimental values may partially be attributed to the fact that our model system does not include spin-flip processes. As shown in Fig. 6, R_P is almost constant for the range of voltage reported here; thus, the bias-dependence of MR is governed by the R_{AP} in the AP-configuration, where the charge

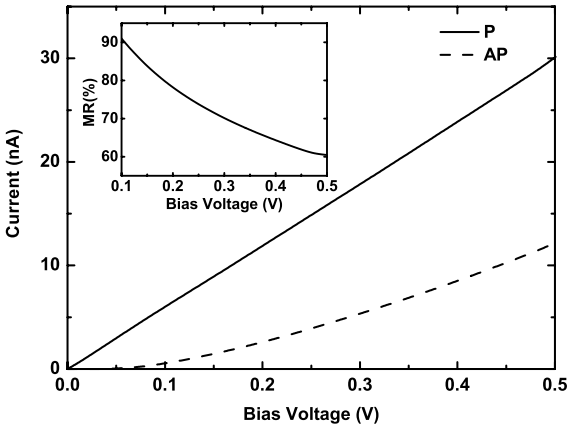

Fig. 6. The I–V characteristic of the OSE spintronics at the conducting state, with the electrochemical potential of $E_P = E_F + 0.8$ eV, in the parallel (solid curve) and antiparallel (dashed curve) configurations. The inset is the MR as the function of bias voltage.

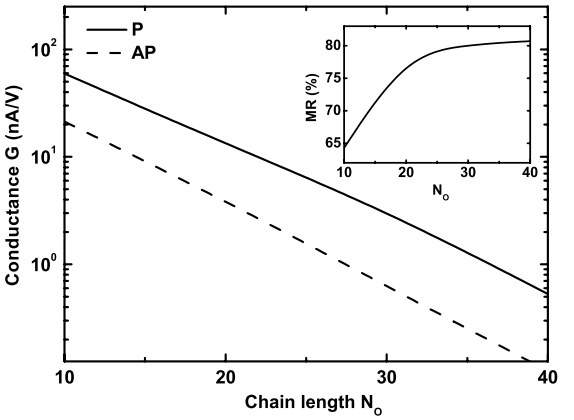

Fig. 7. The length dependence of the conductance in the parallel (solid curve) and antiparallel (dashed curve) configurations, at the bias voltage of $V = 0.4$ V. The inset is the corresponding length dependence of the MR.

carriers in $V > 0$ are the up-spin electrons driven from the full-filled (majority) band of the L-electrode to the half-filled (minority) band of the R-electrode (cf. Fig. 1). As the up-spin electrons traverse the polaron level of the OSE barrier, the electric resistance R_{AP} decreases progressively as the bias voltage increases, resulting in the MR of an appearance of exponential decay.

We now turn to the effect of OSE length on the transport, which has been considered so far only with the fixed value of $N_0 = 10$. The experimental conductance often decreases exponentially as the length of the molecular chain increases [47]. The length-dependent conductance can be investigated theoretically with the help of the equilibrium Green's function formalism [48], and the exponential length dependence of the conductance characterizes the coherent transport [49]. Fig. 7 depicts our theoretical results using the NEGF formalism at the bias voltage $V = 0.4$ V. The evaluated conductances do show near exponential dependences, for both the P- and the AP-configuration. The latter decays faster, leading to the non-uniform OSE-length dependence of MR, as shown in the inset of Fig. 7.

6. Summary and concluding remarks

In summary, we have investigated the spin-dependent charge transport in organic spintronics devices, on the basis of the SSH model combined with the NEGF formalism. We have demonstrated the polaron mechanism for the conductance switching, which can be controlled either by an appropriate bias voltage (Section 3) or by changing the electrode electrochemical potential (Section 4). Despite of its dependence on the electrode property, the conductance switching is generally a property of nanosize organic semiconductors. To have a one- or two-step conductance switching, it is not necessary for the lead to be magnetic. It is believed that the two-step conductance switching can be observed even in some nanostructures with nonmagnetic or paramagnetic electrodes. However, using magnetic electrodes does offer an additional handle on the conductance control (see the discussion to the end of Section 3); thus it has potential applications in organic electronics. We have also studied the behavior of magnetoresistance (Section 5). The calculated magnetoresistance shows an exponential decay as the applied bias voltage increases in the $V > 0$ region. The dependence of the magnetoresistance on the length of molecular junction is also addressed.

It is worth to mention here that a decay behavior of MR has been reported experimentally in an LSMO/OSE(Alq_3)/Co spin-valve device, where the MR has a maximal value at $V \approx 0$ and decreases exponentially as the applied voltage increases [21]. Similar decay behavior is also observed for OSEs with magnetic tunnel junctions with LSMO and Co or CoFe electrodes [50,51]. These experiments are for layer devices with the OSE thicknesses that may lead to the spin-dependent transport of diffusive. The spin diffusion can be incorporated

phenomenologically into the present model to account for the relatively fast decay behavior observed experimentally. It is however beyond the scope of this paper and will be considered elsewhere.

The present calculations are done for the steady or quasi-steady state electric transport. The dynamical polaron effects that are not considered in this work may be importance for the transport in organic spintronics, especially in the presence of a time-dependent external field. Some theoretical investigations have been devoted to this issue. The method used there is the wave-packet evolution approach [52] or non-adiabatic time-dependent Schrödinger equation method [53]. The resulting transport mechanism depends rather sensitively on the time scale of the electronic motion than that of the lattice distortion. Increasing the lattice vibrational frequency, the transport can change from electron-like to polaron-like behavior. The strong lattice fluctuation may also lead to the polaron transport mechanism even in the low phonon-frequency regime [52]. Nevertheless, the polaron mechanism studied in this work for the hysteretic conductance switching and giant magnetoresistance is expected to remain at least qualitatively valid.

Acknowledgement

Support from the National Natural Science Foundation of China (Nos. 10474056 and 10234010) and the Research Grants Council of the Hong Kong Government (No. 605105) is gratefully acknowledged.

References

[1] R. Farchioni, G. Grosso, Organic Electronic Materials, Springer Press, Berlin, 2001.
[2] R.H. Friend, R.W. Gymer, A.B. Holmes, J.H. Burroughes, R.N. Marks, C. Taliani, D.D.C. Bradley, D.A.D. Santos, J.L. Brédas, M. Lögdlund, W.R. Salaneck, Nature 397 (1999) 121.
[3] D. Voss, Nature 407 (2000) 442.
[4] S. Datta, Nanotechnology 15 (2004) S433.
[5] A.R. Rochal, V.M. García-Suárez, S.W. Bailey, C.J. Lambert, J. Ferrer, S. Sanvito, Nat. Mater. 4 (2005) 335.
[6] R.M. Metzger, J. Mater. Chem. 10 (2000) 55.
[7] R.P. Andres, T. Bein, M. Dorogi, S. Feng, J.I. Henderson, C.P. Kubiak, W. Mahoney, R.G. Osifchin, R. Reifenberger, Science 272 (1996) 1323.
[8] W. Liang, M.P. Shores, M. Bockrath, J.R. Long, H. Park, Nature 417 (2002) 725.
[9] I. Kratochvilova, M. Kocirik, A. Zambova, J. Mbindyo, T.E. Malloukc, T.S. Mayer, J. Mater. Chem. 12 (2002) 2927.
[10] K. Walzer, E. Marx, N.C. Greenham, R.J. Less, P.R. Raithby, K. Stokbro, J. Am. Chem. Soc. 126 (2004) 1229.
[11] A.M. Rawlett, T.J. Hopson, I. Amlani, R. Zhang, J. Tresek, L.A. Nagahara, R.K. Tsui, H. Goronkin, Nanotechnology 14 (2003) 377.
[12] N.P. Guisinger, M.E. Greene, R. Basu, A.S. Baluch, M.C. Hersam, Nano Lett. 4 (2004) 55.
[13] C.P. Collier, G. Mattersteig, E.W. Wong, Y. Luo, K. Beverly, J. Sampaio, F.M. Raymo, J.F. Stoddart, J.R. Heath, Science 289 (2000) 1172.
[14] Z.J. Donhauser, B.A. Mantooth, K.F. Kelly, L.A. Bumm, J.D. Monnell, J.J. Stapleton, D.W. Price Jr., A.M. Rawlett, D.L. Allara, J.M. Tour, P.S. Weiss, Science 292 (2001) 2303.
[15] M.A. Reed, J. Chen, A.M. Rawlett, D.W. Price, J.M. Tour, Appl. Phys. Lett. 78 (2001) 3735.
[16] C. Li, W. Fan, B. Lei, D. Zhang, S. Han, T. Tang, X. Liu, Z. Liu, S. Asano, M. Meyyappan, J. Han, C. Zhou, Appl. Phys. Lett. 84 (2004) 1949.
[17] F. Chen, J. He, C. Nuckolls, T. Roberts, J.E. Klare, S. Lindsay, Nano Lett. 5 (2005) 503.
[18] H.X. He, J.H. Zhu, N.J. Tao, J. Am. Chem. Soc. 123 (2001) 7730.
[19] A.S. Blum, J.G. Kushmerick, D.P. Long, C.H. Patterson, J.C. Yang, J.C. Henderson, Y.X. Yao, J.M. Tour, R. Shashidhar, B.R. Ratna, Nat. Mater. 4 (2005) 167.
[20] V. Dediu, M. Murgia, F.C. Matacotta, C. Taliani, S. Barbanera, Solid State Commun. 122 (2002) 181.
[21] Z.H. Xiong, D. Wu, Z.V. Vardeny, J. Shi, Nature 427 (2004) 821.
[22] T. Holstein, Ann. Phys. 8 (1959) 325.
[23] T. Holstein, Ann. Phys. 8 (1959) 343.
[24] J.M. Seminario, A.G. Zacarias, J.M. Tour, J. Am. Chem. Soc. 122 (2000) 3015.
[25] M. Galperin, M.A. Ratner, A. Nitzan, Nano Lett. 5 (2005) 125.
[26] W.P. Su, J.R. Schrieffer, A.J. Heeger, Phys. Rev. B 22 (1980) 2099.
[27] H.J. Torii, J. Phys. Chem. A 104 (2000) 413.
[28] H. Ness, S.A. Shevlin, A.J. Fisher, Phys. Rev. B 63 (2001) 125422.
[29] J.H. Wei, S.J. Xie, S.G. Wang, M.L. Mei, Phys. Lett. A 292 (2001) 207.
[30] E.M. Conwell, S.V. Rakhmanova, Proc. Natl. Acad. Sci. USA 97 (2000) 4556.
[31] J.H. Wei, S.J. Xie, L.M. Mei, J. Berakdar, Y.J. Yan, New J. Phys. 8 (2006) 82.
[32] L.V. Keldysh, Zh. Eksp. Teor. Fiz. 47 (1964) 1515 [Sov. Phys. JETP 20 (1965) 1018].
[33] S. Datta, Electronic Transport in Mesoscopic Systems, Oxford University Press, New York, 1995.
[34] M. Brandbyge, J.L. Mozos, P. Ordejón, J. Taylor, K. Stokbro, Phys. Rev. B 65 (2002) 165401.
[35] S.J. Xie, K.H. Ahn, D.L. Smith, A.R. Bishop, A. Saxena, Phy. Rev. B 67 (2003) 125202.
[36] A. Fert, J. Phys. C: Solid State Phys. 2 (1969) 1784.
[37] R. Landauer, IBM J. Res. Dev. 1 (1957) 223.
[38] R. Landauer, Philos. Mag. 21 (1970) 863.
[39] M.J. McLennan, Y. Lee, S. Datta, Phys. Rev. B 43 (1991) 13846.
[40] A.R. Williams, P.J. Feilbelman, N.D. Lang, Phys. Rev. B 26 (1982) 5433.

[41] D.A. Papaconstantopoulos, Handbook of the Band Structure of Elemental Solids, Plenum Press, New York, 1986.
[42] Z.G. Yu, M.A. Berding, S. Krishnamurthy, Phys. Rev. B 71 (2005) 060408(R).
[43] P.P. Ruden, D.L. Smith, J. Appl. Phys. 95 (2004) 4898.
[44] Z.G. Yu, M. Flatté, Phys. Rev. B 66 (2002) 201202(R).
[45] A.O. Solak, L.R. Eichorst, W.J. Clark, R.L. McCreery, Anal. Chem. 75 (2003) 296–305.
[46] B.Q. Xu, X.Y. Xiao, X.M. Yang, L. Zang, N.J. Tao, J. Am. Chem. Soc. 127 (2005) 2386.
[47] S. Wakamatsu, S. Fujii, U. Akiba, M. Fujihira, Ultramicroscopy 97 (2003) 19.
[48] Y. Asaiand, H. Fukuyama, Phys. Rev. B 72 (2005) 085431.
[49] Y.J. Yan, H.Y. Zhang, J. Theor. Comput. Chem. 1 (2002) 225.
[50] J.M. De Teresa, A. Barthélémy, A. Fert, J.P. Contour, R. Lyonnet, F. Montaigne, P. Seneor, A. Vaurès, Phys. Rev. Lett. 82 (1999) 4288.
[51] J. Hayakawa, K. Ito, S. Kokado, M. Ichimura, A. Sakuma, M. Sugiyama, H. Asano, M. Matsui, J. Appl. Phys. 91 (2002) 8792.
[52] Z.G. Yu, D.L. Smith, A. Saxena, A.R. Bishop, Phys. Rev. B 59 (1999) 16001.
[53] C.Q. Wu, Y. Qiu, Z. An, K. Nasu, Phys. Rev. B 68 (2003) 125416.